Journal of Power Sources 242 (2013) 455–463

Contents lists available at SciVerse ScienceDirect

Journal of Power Sources

journal homepage: www.elsevier.com/locate/jpowsour

Vertically aligned nanocomposite electrolytes with superior out-of-plane ionic conductivity for solid oxide fuel cells

Qing Su [a], Daeil Yoon [b], Aiping Chen [c], Fauzia Khatkhatay [c], Arumugam Manthiram [b], Haiyan Wang [a,c,*]

[a] Material Science and Engineering Program, Texas A&M University, College Station, TX 77843-3128, USA
[b] Electrochemical Energy Laboratory & Materials Science and Engineering Program, University of Texas at Austin, Austin, TX 78712, USA
[c] Department of Electrical and Computer Engineering, Texas A&M University, College Station, TX 77843-3128, USA

HIGHLIGHTS

- YSZ/GDC VAN electrolyte is achieved with tunable vertical grain boundary densities.
- This electrolyte provides superior out-of-plane ionic conductivity.
- The enhancements come from vertically aligned interfaces or vertical strain.
- The power output of fuel cells significantly increases by applying VAN electrolyte.

GRAPHICAL ABSTRACT

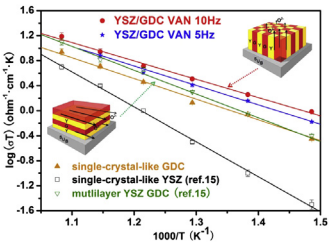

ARTICLE INFO

Article history:
Received 13 March 2013
Received in revised form
23 May 2013
Accepted 25 May 2013
Available online 4 June 2013

Keywords:
Vertically aligned nanocomposite electrolyte
Ionic conductivity
Pulsed laser deposition
Vertical interface
Interfacial strain

ABSTRACT

Two-phase $(Ce_{0.9}Gd_{0.1}O_{1.95})_{0.5}/(Zr_{0.92}Y_{0.08}O_{1.96})_{0.5}$ (GDC/YSZ) nanocomposite thin films with vertically aligned structure are grown as the electrolyte for thin film solid oxide fuel cells (TFSOFCs). X-ray diffraction (XRD) and transmission electron microscopy (TEM) results confirm that GDC and YSZ grow as separated, high crystallinity nanocolumns with tunable column width on both single crystal and polycrystalline anode substrates. Impedance measurements demonstrate ~50% enhancement in ionic conductivity compared to pure single-crystal-like GDC thin film. The enhanced properties in the GDC/YSZ vertically aligned nanocomposite (VAN) system may be attributed to two-phase strain coupling and the fast ionic transport rate along the vertical interfaces. The VAN is applied in thin film SOFC as a part of the electrolyte in the single cells. The overall power density increases more than 40% compared with that of the cells without VAN electrolyte. This work demonstrates the first VAN nanostructured electrolyte with the essential vertical ion-transport channels. The new VAN electrolyte provides superior out-of-plane ionic conductivity compared to those single phase electrolytes as well as the nanolayered electrolytes.

1. Introduction

Because of their high efficiency and wider range of fuel options, thin film solid oxide fuel cells (TFSOFCs) have attracted extensive research interests [1–4]. The main issue for SOFCs is to achieve desired cell performance at intermediate temperatures (600–800 °C) or lower [1]. However, the ionic conductivity of the electrolyte decreases significantly at low temperatures, leading to low power density. The most promising way to decrease the ohmic loss of the electrolyte at low temperatures is to reduce the electrolyte thickness, which, however, may raise concerns about the durability and mechanical stability of the electrolyte. Therefore, exploring higher conductivity electrolytes is critical for developing low-temperature (LT) SOFCs [3].

Following the widely used Yttria stabilized zirconia (YSZ), [5,6] much work has been done to investigate various alternative

* Corresponding author. Department of Electrical and Computer Engineering, Texas A&M University, College Station, TX 77843-3128, USA. Tel.: +1 979 845 5082.
E-mail address: wangh@ece.tamu.edu (H. Wang).

0378-7753/$ – see front matter © 2013 Elsevier B.V. All rights reserved.
http://dx.doi.org/10.1016/j.jpowsour.2013.05.137

electrolytes, among which aliovalent-doped ceria (doped CeO_2) and isovalent-cation–stabilized bismuthoxides have attracted much attention because of their superior ionic conductivity at low temperatures [7,8]. Unfortunately, the higher conductivity comes at the expense of thermodynamic instability, which raises the concern about the electrolyte reliability. Besides material exploration, material nanostructure engineering provides another possibility to enhance the ionic conductivity. In zirconia and ceria based electrolyte systems, the grain size dependence of conductivity has been investigated and higher ionic conductivity has been observed in nanocrystalline electrolytes [9,10]. On the other hand, the ionic conductivity of YSZ thin film was found to increase when the film thickness decreases to below 30 nm, which demonstrates an unblocking grain boundary effect [11]. These results suggest that, when the grain size decreases to nanometer range, the ionic conductivity properties of the electrolyte could dominate by interface rather than intragrain.

Based on the above findings, a multilayer strategy (as shown in Fig. 1a) has been applied to create heterogeneous interfaces and is widely used to study the interfacial effect of two ionic conducting systems [12]. A typical example is the two-phase multilayered calcium and barium fluoride (CaF_2 and BaF_2). The fluoride ion conductance was drastically enhanced with increasing interface density, [12] which was attributed to the influence of space charge regions at the interfaces where the carrier density was significantly increased. Besides the two-phase multilayered fluoride systems, the ionic conductivity in multilayered oxide systems including YSZ/$SrTiO_3$ (STO), YSZ/Y_2O_3, YSZ/GDC etc. have also been reported to be enhanced [13–15]. The enhancement in multilayered oxide systems was correlated to the interfacial strain or fast transportation along interface rather than the space charge regions at the interfaces [13,15]. This provides possibility to create fast transportation channels (interfaces) or tune the interfacial strain to enhance the ionic conductivity. Generally, the transportation parallel to the grain or phase boundaries is strongly enhanced, while the transportation across the grain or phase boundaries is blocked for oxide systems [16]. Overall, the multilayer strategy helps to facilitate the diffusion along the parallel interfaces, but has limited impact on the transport property in the out-of-plane direction that is required for the oxygen ion transport in SOFCs.

To achieve enhanced vertical transport properties in electrolyte, self-assembled vertically aligned nanocomposite (VAN) structure with vertical interfaces is proposed and illustrated in Fig. 1b. Various VAN systems have been demonstrated in functional oxides for multiferroics, [17,18] low field magnetoresistance materials, [19,20] and others [21,22]. Because the interface area within the composite is much larger than the contact area of each nanocolumn with the substrate, the VAN systems are free from substrate clamping constraints and are mainly controlled by vertical strain. This provides enormous potential to control strain vertically in much thicker films with correspondingly large volume [17].

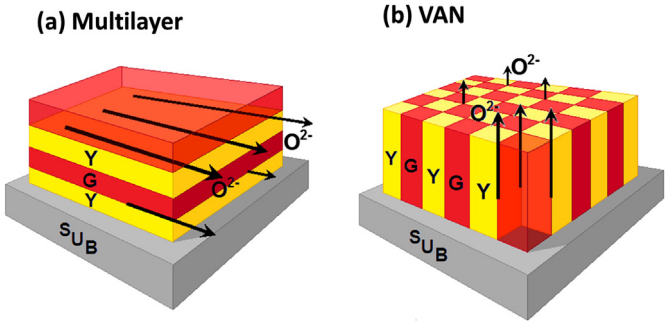

Fig. 1. (a) Illustration of a conventional thin-film multilayers strategy with lateral interfaces to enhance the in-plane ionic conductivity where "Y" and "G" stands for YSZ and GDC electrolyte, respectively. (b) Schematic diagram of a self-assembled vertically aligned nanocomposite (VAN) film with vertically aligned interfaces to increase the out-of-plane ionic transportation.

In this paper, Pulsed laser deposition (PLD) is used to fabricate a unique YSZ/GDC VAN structure in one-step on both single crystalline STO (001) and polycrystalline NiO-YSZ substrates based on the spontaneous phase ordering. The ionic conductivity of the VAN electrolyte is measured and compared with pure YSZ, GDC electrolyte and multilayer YSZ/GDC electrolyte. The possible mechanism for the enhanced ionic transport properties of VAN electrolyte is also proposed. The VAN structure consisting of YSZ/GDC composite as electrolyte is introduced as part of electrolyte to achieve an overall enhancement in power output for SOFCs.

2. Experimental

2.1. Targets and anode disks processing

The PLD targets including $La_{0.5}Sr_{0.5}CoO_{3-\delta}$ (LSCO), 8 mol% yttria stabilized zirconia (YSZ) (500 nm, Tosoh Co.), $Ce_{0.9}Gd_{0.1}O_{1.95}$ (GDC), YSZ and GDC composite, 60 wt. % NiO + 40 wt. % YSZ (NiO-YSZ, 500 nm, Praxair Inc) anode disks were all fabricated by solid state reaction through mixing stoichiometric amounts of the raw powders: La_2O_3 (99.99%), $SrCO_3$, Co_3O_4 (99.9%), CeO_2 (99.9%), YSZ and Gd_2O_3 (99.9%). The sintering details can be found elsewhere [23]. YSZ and GDC composite target was sintered at 1100 °C for 12 h in oxygen. The phase purity of LSCO and GDC/YSZ composite targets were confirmed by X-ray diffraction (XRD).

2.2. Thin film preparation

Platinum thin layers (~100 nm) were sputtered both on single crystal $SrTiO_3$ (STO) (001) substrates as bottom electrode and on YSZ and GDC composite thin films as top contact. The YSZ and GDC composite thin films were deposited on single crystal $SrTiO_3$ (STO) (001) substrates and Pt-sputtered STO substrates in a PLD system with a KrF excimer laser (Lambda Physik Compex Pro 205, $\lambda = 248$ nm). The deposition frequency varied from 1 Hz to 10 Hz to optimize the column width and interface density. The laser beam with approximately 5 J cm^{-2} in energy density was focused on the targets at a 45° incidence angle. An optimized substrate temperature of 700 °C and oxygen pressure of 26 Pa was employed for the depositions. After the deposition, the films were cooled down at 10 °C min^{-1} under oxygen pressure of 26 kPa to assure proper film stoichiometry. The phase and orientation of the films were examined by XRD (θ–2θ scan with Cu Kα radiation, $\lambda = 1.5406$ Å, Bruker D8 Discover X-ray powder diffractometer).

2.3. Single cells fabrication

To prepare the anode-supported single cells, commercial NiO-YSZ cermet powder was compacted into anode disks under uniaxial pressure using a die set of 1 inch (2.54 cm) in diameter. The disks were then sintered at 1300 °C for 3 h. Thin film electrolytes were coated by PLD with a growth rate of ~0.8, ~0.9 and ~0.9 Å s^{-1} for YSZ, GDC and YSZ/GDC VAN layers separately. The YSZ layer thickness was kept ~1.5 μm for all single cell samples. The pure GDC layer with the thickness of ~4.5 μm was coated as the reference sample. To study the electrolyte architecture effect on overall power density, the GDC and YSZ/GDC VAN electrolyte were coated with different sequences by keeping the total thickness of GDC and YSZ/GDC VAN electrolyte ~4.5 μm. A screen printed LSCO cathode layer was then screen printed onto a NiO-YSZ anode disk substrate. All of the cells were annealed at

1150 °C for 2 h with a ramping rate of 2 °C min^{-1} to ensure fair comparison.

2.4. Microstructure and electrochemical properties characterization

The microstructure of these films was first characterized by a high resolution field emission scanning electron microscope (FE-SEM, JEM-7500F Cold Emission SEM) and by transmission electron microscopy (TEM) (JEOL JEM-2010 and FEI Tecnai G2 F20 operated at 200 kV). Cross-sectional and plan-view samples for TEM analysis were prepared by a standard manual grinding and thinning procedure followed by a final polishing step in a precision ion polishing system (PIPS 691, Gatan). STEM was conducted on the FEI Tecnai F20 with a point-to-point resolution of 0.27 nm.

Platinum grids were gently pressed onto Pt top contacts and were used as current collectors. Using a potentiostat/impedance analyzer (Reference 600™, Potentionstat/Galvanstat/ZRA, GAMRY INSTRUMENTS), AC impedance spectroscopy measurements were conducted in the frequency range of 10^{-1}–3×10^5 Hz in the temperature range from 400 to 700 °C. The AC impedance data were measured after a waiting period of an hour for temperature stabilization. The anode-supported single cells prepared with and without the interlayer were used to evaluate the VAN electrolyte effect on the single cell performance. Humidified H_2 with a constant flow rate of 80 mL min^{-1} and air with at a constant flow rate of 120 mL min^{-1} were supplied as the fuel and the oxidant, respectively, during single-cell performance test.

3. Results and discussion

The XRD pattern of the YSZ and GDC composite target is shown in Fig. 2a. The diffraction peaks of GDC and YSZ reveal the typical fluorite structure of GDC and YSZ, [24] indicating no obvious solid state reaction between GDC and YSZ. Fig. 2b shows the XRD θ–2θ patterns of pure STO substrate and a typical YSZ and GDC nanocomposite film deposited at 10 Hz. The (002) peaks for GDC and YSZ slightly overlap as a possible result of the vertical strain coupling between the two phases. It can be clearly seen that only the (002) peaks of both the GDC and YSZ phases are observed, indicating that both phases have grown highly textured along (00l) on the STO (001) substrate. Considering the lattice parameter for STO, YSZ and GDC is 3.91 Å, 5.13 and 5.41 Å, respectively, YSZ and GDC will prefer an epitaxial cubic on cubic growth with a 45° in-plane rotation with STO substrate in order to minimize the lattice mismatch (as illustrated in Fig. 2c). The epitaxial growth of YSZ/GDC composite on STO results in the preferred (001) out-of-plane texture. Several small peaks, which are also observed in the baseline scan on STO single crystalline substrates, are marked in the XRD profile as background peaks from the substrate and the XRD holder.

TEM was conducted to examine the microstructure of films deposited under different deposition frequencies. Fig. 3a and b show the cross-sectional TEM images for the YSZ/GDC nanocomposite films on the STO (001) deposited at 1 Hz and 10 Hz, respectively. It can be seen that the sub-20 nm epitaxial growth of YSZ and GDC columns are vertically aligned on the substrate, indicating the self-assembled VAN structures. It could be seen that

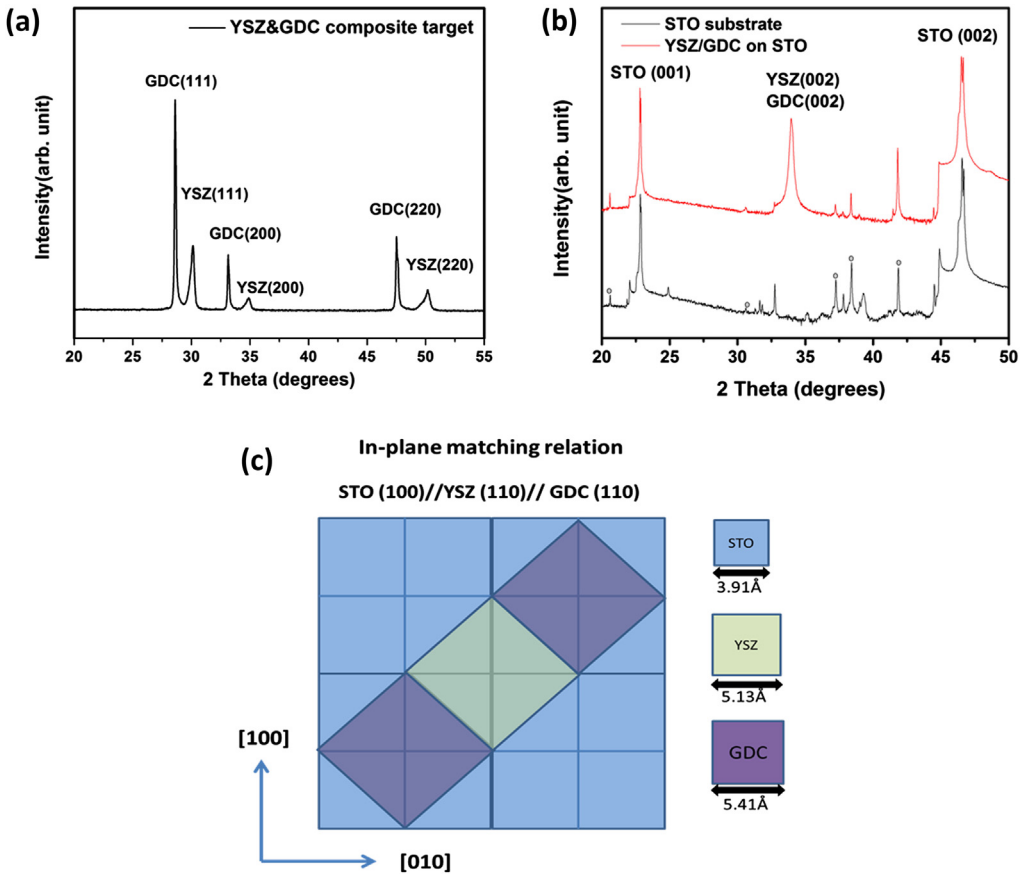

Fig. 2. X-ray diffraction (XRD) patterns of (a) the YSZ and GDC composite target showing no inter-reaction between YSZ and GDC and (b) pure STO substrate and a typical YSZ/GDC nanocomposite film deposited at 10 Hz showing an epitaxial growth of YSZ/GDC nanocomposite film. (c) Illustration of YSZ and GDC with a 45° in-plane rotation matching on STO substrate.

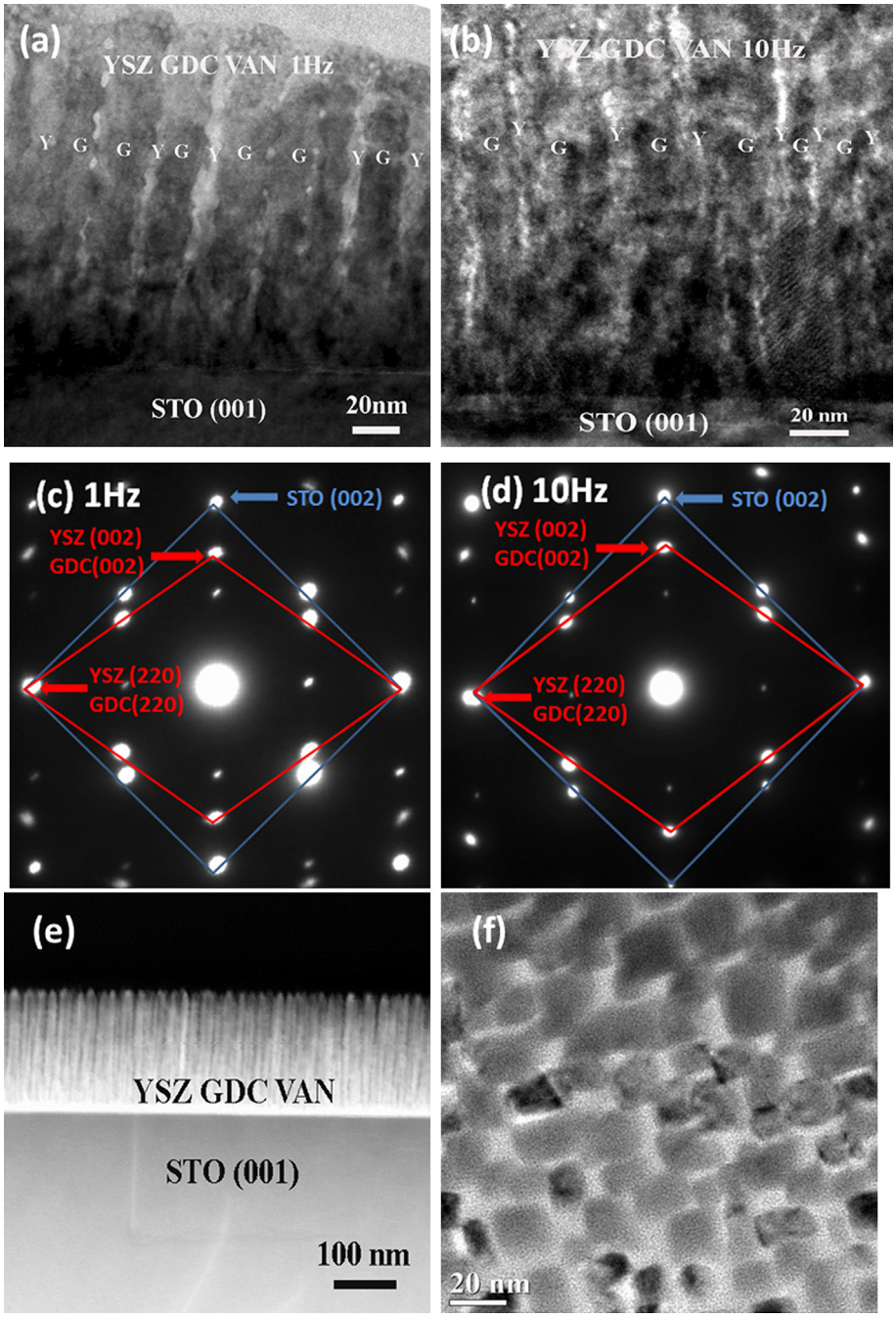

Fig. 3. Cross-sectional TEM images for the YSZ/GDC nanocomposite films on STO(001) deposited at (a) 1 Hz and (b)10 Hz, which clearly demonstrate different column sizes by different deposition frequencies. The selected area electron diffraction (SAED) patterns of YSZ/GDC nanocomposite films on STO(001) deposited at (c) 1 Hz and (d)10 Hz indicating a 45° rotation matching on STO substrate. The cross-sectional STEM images (e) and (f) plan-view TEM images of YSZ and GDC nanocomposite thin film show the phase separation and arrangement.

the average column width decreases as the deposition frequency increases due to the reduced diffusion length of the adatoms as deposition frequency increases. Fig. 3c and d are the corresponding selected area electron diffraction (SAED) patterns of Fig. 3a and b. The orientation relations between both of the YSZ/GDC nanocomposite films and the substrates are determined to be YSZ (002)/GDC (002)/STO (002), and YSZ [220]/GDC [220]/STO [200]. This in-plane 45° rotation enables a better lattice matching of YSZ and GDC with the underlying STO (a = 3.905 Å). The relative strain (ε) is estimated from the equation: $\varepsilon = \alpha - \alpha_{bulk}/\alpha_{bulk}$, where α_{bulk} is the lattice constant of unstrained bulk material (For GDC a = 5.418 Å, and for YSZ, a = 5.147 Å). The out-of-plane lattice parameters of YSZ and GDC are calculated as 5.27 Å and 5.28 Å based on the XRD and SAED patterns. The YSZ/GDC VAN electrolyte results in a ~2.6% compressive strain for GDC and a ~2.2% tensile strain for YSZ out-of-plane.

To confirm that YSZ and GDC grow as alternating columns without intermixing, scanning transmission electron microscopy (STEM) was conducted under a high-angle annular dark field (HAADF) condition, where the contrast is roughly proportional to atomic number square (Z^2, also called Z-contrast imaging). A typical Z-contrast image over a large area of YSZ/GDC VAN structure is

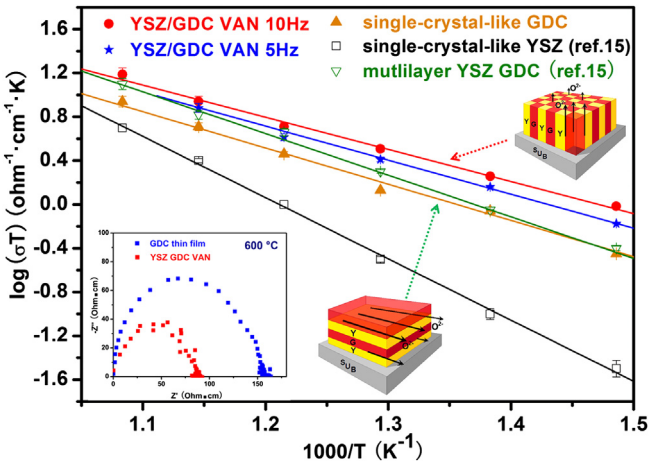

Fig. 4. An Arrhenius plot of ionic conductivity as a function of temperature showing enhanced ionic conductivity for YSZ/GDC VAN electrolyte compared to pure GDC and YSZ thin film. The inset is a specific impedance plot of GDC film and YSZ and GDC VAN film at 600 °C.

shown in Fig. 3e. Because of the higher Z numbers of Ce and Gd, GDC columns have much higher contrast (brighter columns) than YSZ columns. The GDC and YSZ grains grow into well-aligned vertical columns and alternate with each other with a column size of ~5–15 nm. Energy dispersive X-ray (EDX) line scan was conducted over the same area (not shown here), and no obvious intermixing was observed. The plan-view TEM in Fig. 3f shows the nanoscale checkerboard-like microstructure of YSZ/GDC nanocomposite film, indicating a spontaneous phase ordering of the two phases.

In order to measure the electrochemical characteristics and test the performance of the VAN electrolyte, multilayer samples of Pt/VAN/Pt on STO (001) substrates were prepared. The total VAN electrolyte thickness is about 1 μm. The inset of Fig. 4 shows the typical impedance spectra measured in air at 600 °C for pure GDC thin film and YSZ/GDC VAN thin films. A model containing two single RC elements (i.e., a resistor (R) in parallel with a capacitor (C)) is used as the equivalent circuit to obtain the impedance–frequency relation at various temperatures. The high frequency impedance arc of the thin films is ascribed as the total contribution of grains and grain boundaries of the electrolyte ionic resistivity. The low frequency semicircle corresponds to the Pt electrode which is used as current collector for the measurement. The ionic conductivity dominates in these materials including YSZ and GDC at the measured temperatures ranges [25]. The thin film ionic conductivity could be calculated as $\sigma_{\text{ionic}} = l/AR$, where σ_{ionic} is the ionic conductivity, R is the thin film resistance, l is the length of the thin film and A is the cross-sectional area. The total ionic conductivity follows the Arrhenius law:

$$\sigma T = \sigma_0 \exp(-E_a/kT) \quad (1)$$

where σ_0, a constant related to the density oxide vacancies, is the pre-exponential factor, E_a is the activation energy for ionic migration and k is the Boltzmann constant.

The Arrhenius plots of ionic conductivity multiply temperature versus reciprocal temperature for GDC thin film and YSZ/GDC VAN thin film are plotted in Fig. 4. The Arrhenius plots of ionic conductivity of the single-crystal-like YSZ thin film and YSZ/GDC multilayer film are also presented for a comparison [15]. Previously, the ionic conductivity multiply temperature of single-crystal-like YSZ thin film and YSZ/GDC multilayer film was reported to be 0.41 and 0.82 Ω^{-1} cm^{-1} K at 600 °C, respectively [15]. In comparison with the ionic conductivity of pure YSZ thin film and pure GDC thin film, the ionic conductivity of the YSZ/GDC VAN thin film is higher for the entire temperature range by applying the VAN microstructure. Both the VAN samples deposited with different frequencies show enhanced conductivity, *e.g.*, ionic conductivities multiply temperature for 5 Hz and 10 Hz samples are 0.88 and 0.96 Ω^{-1} cm^{-1} K at 600 °C, respectively. The higher the deposition frequency for the VAN electrolyte, the higher the ionic conductivity is. Since the vertically aligned interface density increases as deposition frequency increases, the result indicates that the ionic conductivity properties of VAN electrolyte dominate by interfaces rather than intragrain. It is also observed that the activation energy for the VAN electrolyte film is lower than that for the pure YSZ and GDC film, indicating lower oxygen ion migration energy for the VAN electrolyte film, thus may benefit its application in LT SOFCs.

The maximum value for the ionic conductivity appears to be at least 2 times higher than that of single-crystal-like YSZ thin film and ~50% higher than that of single-crystal-like GDC thin film reported. Since there are strong indications of carrier depletion for YSZ and GDC oxide systems with increasing interface density and the Debye screening length is inversely proportional to the square root of the carrier density which is only ~0.1 nm in this system, [16,26] the enhanced oxide ion conductance may be resulting from the lattice strain near the layer interfaces or high oxide ion mobility along the interface. Fig. 5a is the high resolution TEM (HRTEM) micrograph showing the vertical interface between YSZ and GDC.

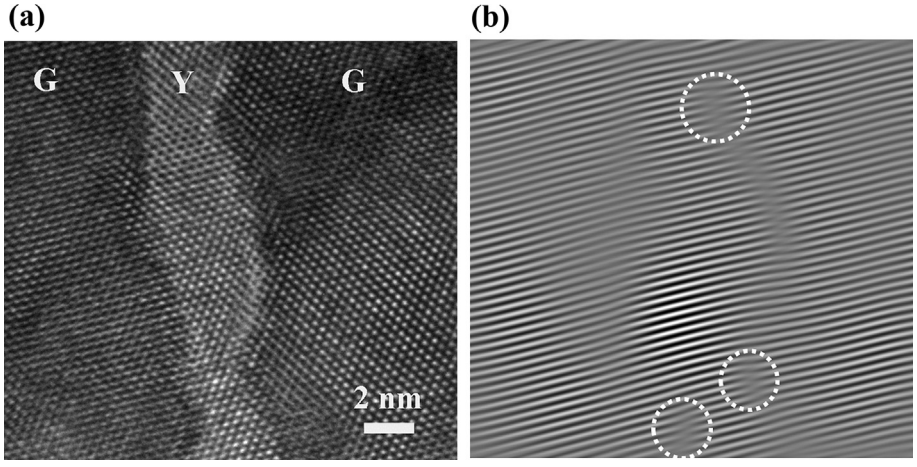

Fig. 5. (a) Cross-sectional HRTEM image of YSZ/GDC VAN thin film and (b) its corresponding FFT image suggest the strain coupling along the vertical YSZ/GDC interfaces.

To better illustrate the dislocation features at the interface, Fourier-filtered image of HRTEM is shown in Fig. 5b. The interface dislocations are identified by the dashed-line circles in the filtered image. The dislocation density is similar at each YSZ/GDC interface regardless of the number of interfaces in these films. Those vertical interfaces with extended defects due to the lattice mismatch may *provide* fast channels for oxide ion transportation out-of-plane. Besides the interfaces, the lattices strain may also play a role. For the oxide ion conductor including YSZ, GDC and etc., there is an exponential dependence of the ionic conductivity σ_o^{2-}int in the ionic conductor close to the interface on the migration volume ΔV_v^M of vacancies and on the lattice misfit f_{12}:

$$\ln\left(\sigma_o^{2-}\text{int}/\sigma_o^{2-}\text{vol}\right) \sim \Delta V_v^M f_{12} \quad (2)$$

where σ_o^{2-}int/σ_o^{2-}vol is the ratio of ionic conductivity of the interface regime and the bulk [27]. For oxide systems including YSZ, GDC etc., which have a vacancy-type diffusion mechanism, the migration volume is usually positive. [28] Thus, the tensile strain has a positive effect on the interfacial ionic conductivity for YSZ and GDC systems which were also demonstrated by previous work [29,30]. In this work, there are 2.6% out-of-plane compressive strain for each GDC column and a 2.2% out-of-plane tensile strain for each YSZ column. The overall ionic conductivity enhancement may be resulted from both higher ionic transporting along vertical interfaces and the strain effects within the two vertical phases in which the fast ionic transport along the interlayer plays a dominant role. Considering the ionic resistance for YSZ is higher than that of GDC, the increase of ionic conductivity of YSZ from tensile strain may exceed the decrease of ionic conductivity of GDC due to the compressive strain. Therefore, an overall enhanced ionic conductivity for YSZ/GDC VAN electrolyte is observed. The vertical strain could be further optimized by the composition and column width.

To demonstrate the VAN electrolyte effect on the overall cell performance, anode-supported single cells with and without the VAN electrolyte were prepared. As seen from the cross-sectional backscattered SEM images of single cells with the VAN electrolyte, the dense and crack-free electrolytes were successfully prepared on porous NiO-YSZ anodes. A single cell with the bi-layer electrolyte of YSZ (~1.5 μm) and GDC (~4.5 μm) (without VAN layer) is used as a reference sample [31]. The single cells with VAN electrolytes applied either in the middle of YSZ and GDC electrolyte (Fig. 6a) or on top of YSZ and GDC electrolyte (Fig. 6b) were prepared to optimize the electrolyte structure. The columnar feature with different contrasts is observed for the VAN electrolyte layer. A YSZ thin layer is applied to prevent the reduction of Ce^{4+} into Ce^{3+} which occurs in hydrogen atmosphere and leads to the decrease of open circuit voltage (OCV) [32].

The growth of dual-phase electrolyte mainly involves two stages, the clusters nucleation and film growth. At the very early stage of composite film growth, different adatoms will arrive at the substrate surface simultaneously. Same phase molecules will accumulate and nucleate to minimize the total system free energy. The phase column widths are determined by the adatoms' diffusivity as a competition. The following film growth will perform as homogeneous phase growth mode in vertical and heterogeneous growth in lateral, defined by the energy minima and to reduce the lattice mismatch.

Compared with the vertically-aligned dual phase structure achieve on single crystal substrate, alternating columns can be achieved on polycrystalline anode substrate either in perfectly vertically-aligned or tilted at a certain angle as seen in the illustration in Fig. 7a. To confirm, cross-sectional TEM has been conducted on the YSZ/GDC composite electrolyte on polycrystalline anode substrate. Fig. 7b is the TEM image of the top portion of YSZ/GDC composite electrolyte on NiO-YSZ polycrystalline anode substrate coated with YSZ and GDC. The alternating columns with different contrasts indicate that dual-phase solid electrolyte has an alternating columnar growth and the VAN-like microstructure could extend to over micron range. Perhaps due to the surface roughness of polycrystalline substrate, the nanocolumns are either vertically-aligned or tilted at a certain angle which demonstrates that a VAN-like microstructure has been successfully fabricated on a polycrystalline anode substrate regardless of the surface roughness. Fig. 7c is the high resolution TEM image of selected area in Fig. 7b. The alternating sub-20 nm columns are observed where the average column width of GDC is ~13 nm and average column width of YSZ is ~ 5 nm. Those results have been further confirmed by the STEM study in Fig. 7d where different contrasts of columns can be seen, demonstrating two-phase structure without obvious intermixing. It is found that the average column width obtained from TEM images is smaller than that obtained from backscattered SEM image possibly because of the resolution limitation of SEM, i.e., one column observed in SEM may contain several nanocolumns identified by TEM.

A nanoporous LSCO cathode layer has been applied between the electrolyte and screen printed LSCO cathode to improve the electrochemical performance of the cathode layer as well as the overall cell performance and cell integrity [31,33]. A heating

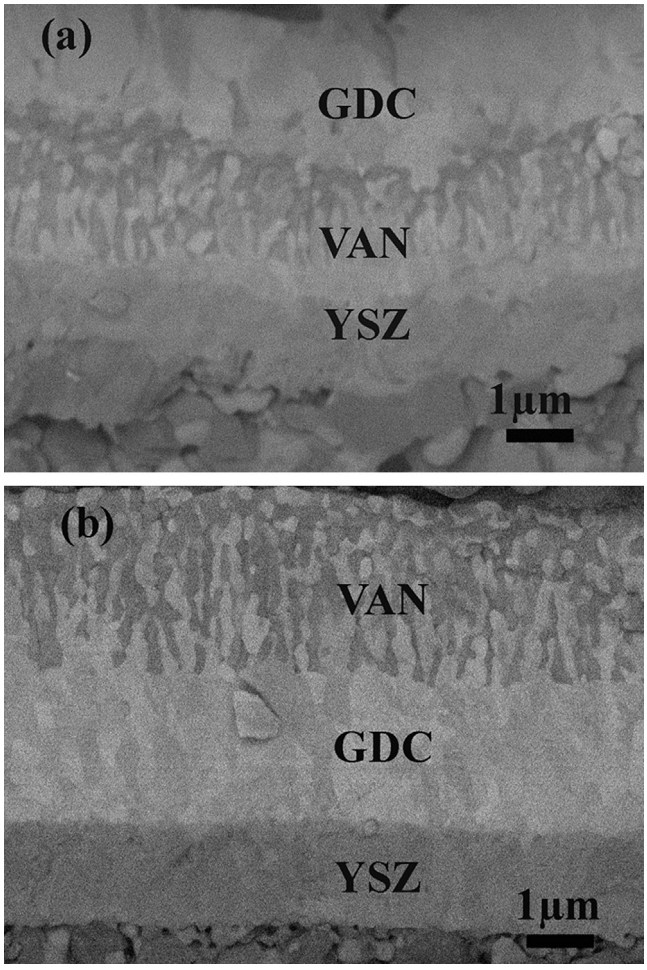

Fig. 6. Cross-sectional backscattered SEM images of single cells with VAN electrolyte (a) in the middle of YSZ and GDC electrolyte and (b) on the top of YSZ and GDC electrolyte.

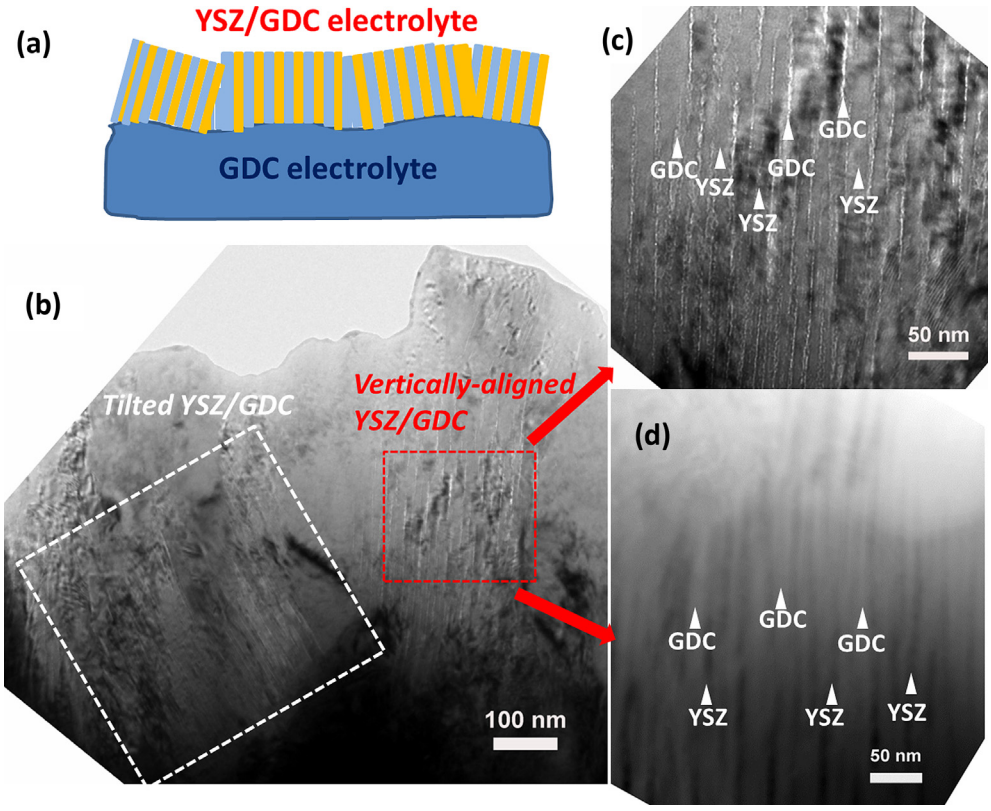

Fig. 7. (a) Schematic illustration of YSZ/GDC composite electrolyte coated on polycrystalline substrate, (b) cross-sectional TEM image of YSZ/GDC composite electrolyte coated on polycrystalline substrate showing alternating YSZ and GDC columns either vertical aligned or slightly tilted, (c) high resolution TEM image and (d) STEM image of YSZ/GDC composite electrolyte demonstrating dual-phase electrolyte without formation of solid solution.

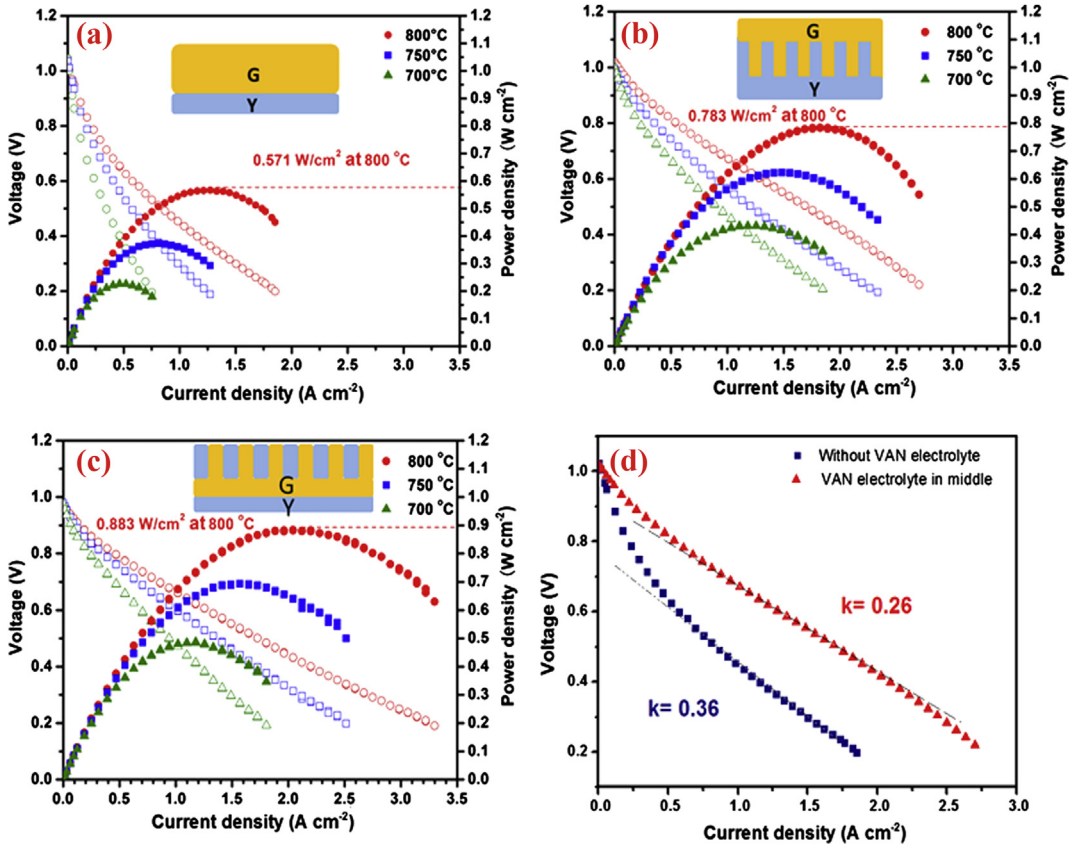

Fig. 8. The power densities of single cells (a) without VAN, (b) with VAN in middle of the electrolyte and (c) on the top of the electrolyte, demonstrating the enhanced cell performance by applying VAN electrolyte. (d) The *V*–*I* curve of the single cells with VAN electrolyte in middle and without VAN electrolyte at 800 °C.

treatment at 1150 °C for 2 h is adopted to ensure the adhesion for the screen printed cathode. Concerning the possible formation of CeO_2–ZrO_2 solid solution, there could be some minor Ce^{4+} diffusion into YSZ matrix based on a previous study [24]. However the two phase separation in the YSZ and CGO VAN structure is evident based on TEM, STEM and backscattered SEM images in Figs. 3, 6 and 7, respectively, for the VAN samples grown on STO and polycrystalline substrates. Therefore, it is believed that the diffusion is minor and it does not significantly affect the cell performance.

The current–voltage (*I–V*) characteristics of the anode-supported single cells with and without the VAN electrolyte were measured using a two-electrode set-up. Pt wires were used as electrical contacts held by Pt paste. The cell performance was measured at the temperatures ranging from 700 to 800 °C. The cell voltage and power density as a function of current density for the sample without VAN electrolyte is shown in Fig. 8a. The open circuit voltage (OCV) is 1.03 V at 700 °C and the maximum power densities of the cell are 0.227, 0.376 and 0.571 W cm^{-2} (highlighted with red arrow) at 700, 750 and 800 °C, respectively. The overall trend is that the cell potential decreases as a result of the increasing polarization losses across the cell with increasing current density, and the power density also decreases as the operating temperature decreases. The cell with the YSZ/GDC VAN electrolyte applied in the middle of YSZ and GDC electrolyte (i.e., YSZ/VAN/GDC) (Fig. 6a) provides an OCV of 1.04 V at 700 °C and the maximum power densities of 0.432, 0.623 and 0.783 W cm^{-2} (highlighted with red arrow) at 700, 750 and 800 °C, respectively. Compared with the cell without the VAN electrolyte, there is ~40% increase at 800 °C for the cells with the VAN electrolyte in middle. There is a further increase for the fuel cell performance with the VAN electrolyte applied on top of the YSZ and GDC bilayer electrolyte (*i.e.*, YSZ/GDC/VAN) (Fig. 6b) which provides an OCV of 1.01 V at 700 °C and the maximum power densities of 0.488, 0.694, and 0.883 W cm^{-2} (highlighted with red arrow), at, 700, 750, and 800 °C, respectively. The possible reason for the further improvement is that the YSZ/GDC VAN electrolyte enhances the oxygen dissociation and surface oxygen exchange rate at the cathode/electrolyte interface [34]. Compared with the cell without the VAN electrolyte, the cells with the VAN electrolyte at the top show ~90% increase in the overall maximum power density at temperature range from 700 to 750 °C and ~55% increase at 800 °C. It is interesting to observe that applying VAN electrolyte benefits more at lower operation temperatures for SOFCs.

Considering the resistivity of YSZ is higher than that of GDC and VAN, a concern was raised on that the overall electrolyte resistance could be dominated by the YSZ layer. However the overall thickness of the electrolyte is ~6 μm while the YSZ layer thickness is ~1.5 μm and the ionic resistance of YSZ is ~4 times higher than GDC at 700 °C [15]. Therefore both GDC and VAN layers (~4.5 μm in total) in the cells contribute to the overall electrolyte resistivity at the operation temperature range from 700 to 800 °C. More importantly, the overall cell performance enhancement for the cells with VAN is evident and the trend has been repeated in another identical set of three cells (with over 30% power density enhancement by applying VAN electrolyte). The performance enhancement is therefore believed to be mainly resulted by that the VAN electrolyte with vertical interfaces provides fast channels for the oxide-ion diffusion and lower migration energy. The possible reason for the enhancement is that the overall electrolyte resistance decreases by applying VAN electrolyte with superior ionic conductivity. In addition, the high ionic conductivity and low oxide-ion migration energy of VAN electrolyte will result in higher oxide-ion concentration in YSZ electrolyte compared with that in conventional YSZ electrolyte. This could also contribute to the enhanced power output for the cells applying VAN electrolyte.

To further demonstrate that the power output comes primarily from the electrolyte, the power density data of single cells with VAN electrolyte in middle and without VAN electrolyte at 800 °C is plotted and fitted in Fig. 8d. At the Ohmic polarization dominated regimes (current density in the range of ~0.5–~2 A cm^{-2}), the slope could be treated as the Ohmic resistance of the electrolyte. As seen in Fig. 8d, the slope of the electrolyte with VAN in middle is ~30% smaller than that of the conventional single cell with YSZ/GDC bilayer electrolyte. It demonstrates that the improvement is primarily from the electrolyte. Furthermore, the power measurement shows the single cell with YSZ (~1.5 μm) and VAN electrolyte (~4.5 μm) exhibits even higher power density output (for example, 0.957 W cm^{-2} at 800 °C) than the single cells with VAN electrolyte on top and in middle reported in this work. It is evident that the VAN electrolyte could be applied in real cells and enhances the overall power density.

To preliminarily test the durability of YSZ/GDC VAN electrolyte, the post-measurement cross-sectional backscattered SEM images of the single cells with the VAN electrolyte in the middle of the electrolyte stack as well as the top of the electrolyte stack are shown as Fig. 9a and b. No formation of pore or crack is observed and the VAN electrolyte remains its columnar structure after ~2–3 days of power measurements at high temperatures indicating the good high temperature stability properties of the YSZ/GDC VAN electrolyte.

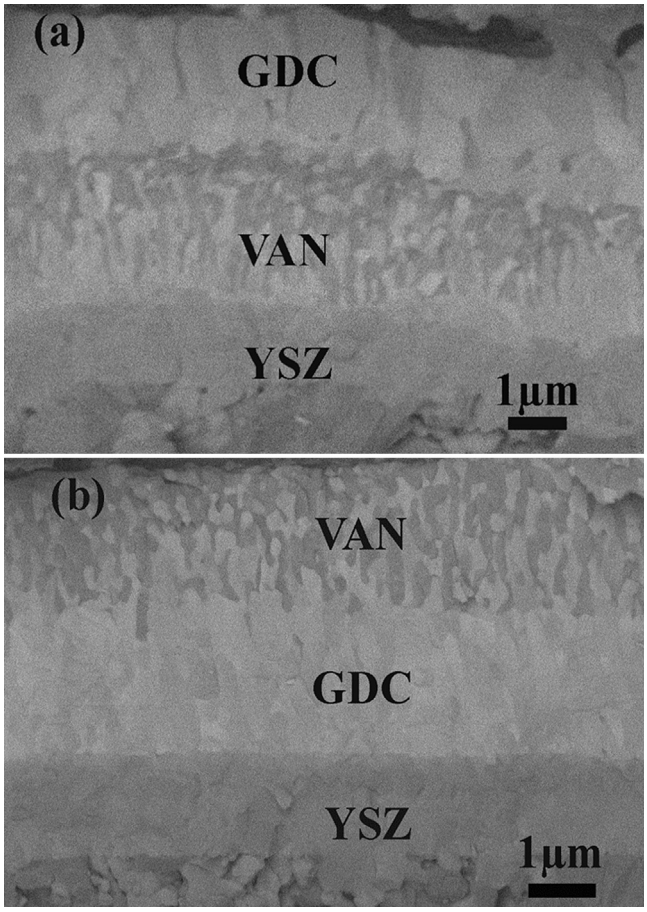

Fig. 9. The post measurement backscattered SEM images of single cell with YSZ/GDC VAN electrolyte (a) in the middle and (b) on the top, showing excellent cell integrity after high temperature cell measurement.

4. Conclusions

YSZ/GDC VAN electrolyte with vertically aligned nanocolumns have been successfully fabricated by PLD. The ionic conductivity of YSZ/GDC VAN electrolyte appears to be at least 2 times higher than that of single crystal like YSZ thin film and 50% higher than that of single crystal like GDC thin film. As the deposition frequency of the YSZ/GDC VAN electrolyte increases, the interface density increases and the ionic conductivity of YSZ/GDC VAN electrolyte improves. The enhanced oxygen ion conductivity may result from lattice strain near the layer interfaces as well as the fast transport path along the vertical interfaces. The anode-supported single cells with YSZ/GDC VAN electrolyte demonstrated enhanced power performance at all temperatures compared with the cells without the VAN electrolyte. Compared with the cell without the VAN electrolyte, the fuel cells with VAN electrolyte show more than 40% increase in the overall maximum power density. Overall, the results strongly support that the YSZ/GDC VAN electrolyte with vertical aligned interfaces improves the ionic conductivity as well as the overall fuel cell performance. Building vertically aligned interfaces provides a novel approach to achieve enhanced ionic conductivity compared to single phase materials and may improve the performance of other electrochemical devices beyond SOFCs.

Acknowledgements

The work was supported by the U.S. National Science Foundation (NSF-0846504 and NSF 1007969). The work at the University of Texas at Austin was supported by the Welch Foundation grant F-1254.

References

[1] S.C. Singhal, Solid State Ionics 135 (2000) 305–313.
[2] A.B. Stambouli, E. Traversa, Renewable and Sustainable Energy Reviews 6 (2002) 433–455.
[3] E.D. Wachsman, K.T. Lee, Science 334 (2011) 935–939.
[4] C. Zuo, S. Zha, M. Liu, M. Hatano, M. Uchiyama, Advanced Materials 18 (2006) 3318–3320.
[5] E. Ivers-Tiffée, A. Weber, D. Herbstritt, Journal of the European Ceramic Society 21 (2001) 1805–1811.
[6] O. Yamamoto, Electrochimica Acta 45 (2000) 2423–2435.
[7] K. Eguchi, T. Setoguchi, T. Inoue, H. Arai, Solid State Ionics 52 (1992) 165–172.
[8] T. Takahashi, T. Esaka, H. Iwahara, Journal of Applied Electrochemistry 7 (1977) 299–302.
[9] T.Y. Tien, Journal of the American Ceramic Society 47 (1964) 430–433.
[10] A. Tschöpe, R. Birringer, Journal of Electroceramics 7 (2001) 169–177.
[11] I. Kosacki, C.M. Rouleau, P.F. Becher, J. Bentley, D.H. Lowndes, Solid State Ionics 176 (2005) 1319–1326.
[12] N. Sata, K. Eberman, K. Eberl, J. Maier, Nature 408 (2000) 946–949.
[13] J. Garcia-Barriocanal, A. Rivera-Calzada, M. Varela, Z. Sefrioui, E. Iborra, C. Leon, S.J. Pennycook, J. Santamaria, Science 321 (2008) 676–680.
[14] C. Korte, A. Peters, J. Janek, D. Hesse, N. Zakharov, Physical Chemistry Chemical Physics 10 (2008) 4623–4635.
[15] S. Azad, O.A. Marina, C.M. Wang, L. Saraf, V. Shutthanandan, D.E. McCready, A. El-Azab, J.E. Jaffe, M.H. Engelhard, C.H.F. Peden, S. Thevuthasan, Applied Physics Letters 86 (2005).
[16] X.X. Guo, J. Maier, Advanced Materials 21 (2009) 2619–2631.
[17] J.L. MaCmanus-Driscoll, P. Zerrer, H.Y. Wang, H. Yang, J. Yoon, A. Fouchet, R. Yu, M.G. Blamire, Q.X. Jia, Nature Materials 7 (2008) 314–320.
[18] Z.X. Bi, J.H. Lee, H. Yang, Q.X. Jia, J.L. MacManus-Driscoll, H.Y. Wang, Journal of Applied Physics 106 (2009).
[19] A.P. Chen, Z.X. Bi, C.F. Tsai, J. Lee, Q. Su, X.H. Zhang, Q.X. Jia, J.L. MacManus-Driscoll, H.Y. Wang, Advanced Functional Materials 21 (2011) 2423–2429.
[20] A.P. Chen, Z.X. Bi, H. Hazariwala, X.H. Zhang, Q. Su, L. Chen, Q.X. Jia, J.L. MacManus-Driscoll, H.Y. Wang, Nanotechnology 22 (2011).
[21] S.A. Harrington, J.Y. Zhai, S. Denev, V. Gopalan, H.Y. Wang, Z.X. Bi, S.A.T. Redfern, S.H. Baek, C.W. Bark, C.B. Eom, Q.X. Jia, M.E. Vickers, J.L. MacManus-Driscoll, Nature Nanotechnology 6 (2011) 491–495.
[22] Z.X. Bi, E. Weal, H.M. Luo, A.P. Chen, J.L. MacManus-Driscoll, Q.X. Jia, H.Y. Wang, Journal of Applied Physics 109 (2011).
[23] J. Yoon, S. Cho, J.H. Kim, J. Lee, Z. Bi, A. Serquis, X. Zhang, A. Manthiram, H. Wang, Advanced Functional Materials 19 (2009) 3868–3873.
[24] X.D. Zhou, B. Scarfino, H.U. Anderson, Solid State Ionics 175 (2004) 19–22.
[25] N.Q. Minh, Journal of the American Ceramic Society 76 (1993) 563–588.
[26] Y. Chen, J.R. Sellar, Solid State Ionics 86-8 (1996) 207–211.
[27] J.P. Locquet, C. Marchiori, M. Sousa, J. Fompeyrine, J.W. Seo, Journal of Applied Physics 100 (2006).
[28] C. Korte, N. Schichtel, D. Hesse, J. Janek, Monatshefte fur Chemie 140 (2009) 1069–1080.
[29] A. Peters, C. Korte, D. Hesse, N. Zakharov, J. Janek, Solid State Ionics 178 (2007) 67–76.
[30] K.M. Kant, V. Esposito, N. Pryds, Applied Physics Letters 100 (2012).
[31] Q. Su, D. Yoon, Y.N. Kim, W. Gong, A. Chen, S. Cho, A. Manthiram, A.J. Jacobson, H. Wang, Journal of Power Sources 218 (2012) 261–267.
[32] M. Mogensen, N.M. Sammes, G.A. Tompsett, Solid State Ionics 129 (2000) 63–94.
[33] Q. Su, S. Cho, Z. Bi, A. Chen, H. Wang, Electrochimica Acta 56 (2011) 3969–3974.
[34] J.H. Shim, J.S. Park, T.P. Holme, K. Crabb, W. Lee, Y.B. Kim, X. Tian, T.M. Gur, F.B. Prinz, Acta Materialia 60 (2012) 1–7.